

AIMx: An Extended Adaptive Integral Method for the Fast Electromagnetic Modeling of Complex Structures

Shashwat Sharma, *Student Member, IEEE*, and Piero Triverio, *Senior Member, IEEE*

Abstract—Surface integral equation (SIE) methods are of great interest for the efficient electromagnetic modeling of various devices, from integrated circuits to antenna arrays. Existing acceleration algorithms for SIEs, such as the adaptive integral method (AIM), enable the fast approximation of interactions between well-separated mesh elements. Nearby interactions involve the singularity of the kernel, and must instead be computed accurately with direct integration at each frequency of interest, which can be computationally expensive. In this work, a novel algorithm is proposed for reducing the cost-per-frequency associated with near-region computations for both homogeneous and layered background media. In the proposed extended AIM (AIMx), the SIE operators are decomposed into a frequency-independent term, which contains the singularity of the kernel, and a frequency-dependent term, which is a smooth function. The expensive near-region computations are only required for the frequency-independent term, and can be reused at each frequency point, leading to significantly faster frequency sweeps. The frequency-dependent term is accurately captured via the AIM even in the near region, as confirmed through error analysis. The accuracy and efficiency of the proposed method are demonstrated through numerical examples drawn from several applications, and CPU times are significantly reduced by factors ranging from three to 16.

Index Terms—Electromagnetic modeling, surface integral equations, adaptive integral method, fast frequency sweep.

I. INTRODUCTION

FULL-wave electromagnetic modeling is a crucial step in many design workflows, ranging from the characterization of on-chip interconnect networks, to the prediction and synthesis of antenna radiation profiles. The growing complexity of modern electronic and communication devices places a commensurate demand on full-wave simulation tools, especially since device characterization is often required over a wide frequency band.

Volumetric methods such as the finite element method (FEM) [1] and volume integral equations (VIEs) [2]–[4] have proved to be robust, but require a volumetric discretization of conductive and dielectric objects. The FEM additionally requires a discretization of the space in between objects. These requirements lead to systems of equations with a large number

of unknowns. In contrast, surface integral equation (SIE)-based techniques require only a discretization of the surface of conductive and dielectric objects [5]–[10]. However, SIE methods lead to a dense system matrix whose solution is computationally prohibitive for large problems. Techniques based on SIEs heavily rely on various acceleration algorithms [11]–[15], where the system of equations is solved iteratively. The products between a system matrix \mathbf{A} and a vector \mathbf{x} are computed at each iteration as

$$\mathbf{A}\mathbf{x} = \mathbf{A}_{\text{NR}}\mathbf{x} + \mathbf{A}_{\text{FR}}\mathbf{x}, \quad (1)$$

where \mathbf{A}_{NR} and \mathbf{A}_{FR} contain entries of \mathbf{A} corresponding to nearby (“near-region”) and well-separated (“far-region”) mesh elements, respectively. Both \mathbf{A}_{NR} and \mathbf{A}_{FR} depend on the Green’s function of the surrounding medium. The entries of \mathbf{A}_{NR} are dominant, and must be computed accurately with direct integration. Far-region interactions in \mathbf{A}_{FR} are weaker, therefore the product $\mathbf{A}_{\text{FR}}\mathbf{x}$ can be computed in a fast but approximate way, without having to assemble \mathbf{A}_{FR} .

The fast multipole method (FMM) [11], [12] and its multi-level and mixed-form extensions [13], [14] are popular acceleration algorithms. These techniques were developed specifically for the homogeneous medium Green’s function. However, many practical applications involve objects embedded in stratified dielectric media, which may require the more complicated multilayer Green’s function (MGF) [16]. The extension of FMM-based techniques to handle the MGF is not straightforward, and requires either multiple complex exponential terms [17] or numerical integration in the complex plane [18].

Another class of acceleration algorithms arises from the use of an auxiliary coarse grid to compute $\mathbf{A}_{\text{FR}}\mathbf{x}$ quickly. The adaptive integral method (AIM) [15] involves superimposing a regular grid on the structure, and projecting currents and charges from the original mesh onto the auxiliary grid. The translation invariance of the Green’s function is then exploited by using Fast Fourier Transforms (FFTs) to accelerate the computation of $\mathbf{A}_{\text{FR}}\mathbf{x}$. An advantage of the AIM is its kernel-independence, which makes it relatively easy to incorporate the MGF [19]–[22]. The AIM has inspired several related methods, such as the precorrected FFT (pFFT) [23] method, the sparse-matrix/canonical grid (SMCG) [24] method, and several others [25]–[28].

In existing acceleration methods, generating \mathbf{A}_{NR} with direct integration may still have a significant cost, particularly for densely-packed structures with fine features, which often require an extremely fine local mesh. This cost is further

Manuscript received . . . ; revised . . .

S. Sharma and P. Triverio are with the Edward S. Rogers Sr. Department of Electrical & Computer Engineering, University of Toronto, Toronto, ON, M5S 3G4 Canada, e-mails: shash.sharma@mail.utoronto.ca, piero.triverio@utoronto.ca.

This work was supported by the Natural Sciences and Engineering Research Council of Canada (Collaborative Research and Development Grants program), by Advanced Micro Devices, and by CMC Microsystems.

increased in the presence of layered media, since the MGF is significantly more expensive to compute than the homogeneous Green's function. Moreover, since the Green's function is singular when the source and observation points coincide, the entries of \mathbf{A}_{NR} must be computed carefully with advanced singularity extraction or cancellation routines [29], which further add to the computational cost. Finally, the computation of \mathbf{A}_{NR} must be repeated at each frequency of interest. Methods to interpolate simulation results across frequency have been proposed [30]–[34], but still require discrete simulation data at multiple frequencies to gather sufficient sample points. This is particularly onerous for structures whose terminal response varies sharply with frequency, for example due to resonances.

In this contribution, we propose a novel acceleration algorithm based on the AIM, which requires computing \mathbf{A}_{NR} only once for the entire frequency sweep. In the proposed extended adaptive integral method (AIMx), the kernel of each integral operator is carefully decomposed into a frequency-independent term which contains the singularity of the kernel, and a frequency-dependent term which is smooth and nonsingular everywhere in space. This leads to a convenient decomposition of the associated system matrix into frequency-independent and frequency-dependent parts. Through analytical and numerical error analyses, we show that the frequency-dependent part of the system matrix can be accurately interpolated with polynomials even in the near region. Therefore, matrix-vector products involving the frequency-dependent part of each matrix operator are accelerated with the use of FFTs. The frequency-independent part of the matrix is expressed as in (1), where the near-region entries are computed accurately with direct integration. As a consequence, the key advantage of the proposed method is that direct integration needs to be performed only once at the beginning of a frequency sweep, and then can be reused at each frequency point. We describe in detail the proposed matrix decomposition for both the single- and double-layer potential matrix operators [35], for both homogeneous and layered background media. This leads to significantly faster frequency sweeps for a wide range of problems requiring full-wave electromagnetic characterization.

The paper is organized as follows: Section II summarizes the SIE formulation considered and the conventional AIM. Section III provides a detailed description of the proposed method, and Section IV shows analytical and numerical error analyses to support the hypothesis that frequency-dependent terms can be interpolated accurately in the near region. In Section V, we demonstrate the accuracy and efficiency of the proposed method compared to the conventional AIM for a series of numerical examples, including canonical geometries, on-chip devices and large antenna arrays. A discussion of the advantages of the proposed method is given in Section VI, followed by concluding remarks in Section VII.

II. BACKGROUND

Throughout this work, we consider time-harmonic fields. A time dependence of $e^{j\omega t}$ is assumed and suppressed. Vector quantities are written with an overhead arrow, for example $\vec{a}(\vec{r})$. Primed coordinates represent source points, while unprimed coordinates represent observation points. Matrices and

column vectors are written in bold letters, such as \mathbf{A} and \mathbf{x} , while dyadic quantities are denoted with double overbars, as in $\overline{\overline{\mathbf{A}}}$.

A. Formulation

We consider the problem of electromagnetic scattering from a perfect electric conductor (PEC) object to illustrate the proposed method, though it is also applicable to penetrable objects. The surface of the PEC object is denoted as S , with outward unit normal \hat{n} . The conductor is embedded in free space, denoted by \mathcal{V}_0 . The layered medium case will be considered in Section III-C. The unknown induced electric surface current density $\vec{J}(\vec{r})$ on S due to an incident field, $[\vec{E}_{\text{inc}}(\vec{r}), \vec{H}_{\text{inc}}(\vec{r})]$, $\vec{r} \in \mathcal{V}_0$, satisfies the electric field integral equation (EFIE) [29],

$$-j\omega\mu_0 \hat{n} \times \mathcal{L} [\vec{J}(\vec{r}')] (\vec{r}) = \hat{n} \times \vec{E}_{\text{inc}}(\vec{r}), \quad (2)$$

where the single-layer potential operator [35] \mathcal{L} is defined as [29]

$$\begin{aligned} \mathcal{L} [\vec{X}(\vec{r}')] (k_0, \vec{r}) \\ = \int_S \left(\vec{X}(\vec{r}') + \frac{1}{k_0^2} \nabla' \nabla' \cdot \vec{X}(\vec{r}') \right) G(k_0, \vec{r}, \vec{r}') dS. \end{aligned} \quad (3)$$

In (2) and (3), ω is the cyclical frequency, μ_0 and k_0 are the permeability and wave number of free space, respectively, and the kernel $G(k_0, \vec{r}, \vec{r}')$ is the free space Green's function,

$$G(k_0, \vec{r}, \vec{r}') = \frac{e^{-jk_0 r}}{4\pi r}, \quad (4)$$

where $r = |\vec{r} - \vec{r}'|$.

Next, a triangular mesh is generated for S , and (2) is discretized with the method of moments (MoM). The electric surface current density $\vec{J}(\vec{r})$ is expanded with Rao-Wilton-Glisson (RWG) basis functions [36] defined on pairs of adjacent triangles, and (2) is tested with $\hat{n} \times$ RWG basis functions to get the matrix equation

$$-j\omega\mu_0 \left(\mathbf{L}^{(A)} + \frac{1}{k_0^2} \mathbf{L}^{(\phi)} \right) \mathbf{J} = \mathbf{E}_{\text{inc}}, \quad (5)$$

where $\mathbf{L}^{(A)}$ and $\mathbf{L}^{(\phi)}$ are, respectively, the vector and scalar potential parts of the discretized $\hat{n} \times \mathcal{L}$ operator. Column vectors \mathbf{J} and \mathbf{E}_{inc} contain coefficients of the basis functions associated with $\vec{J}(\vec{r})$ and $\hat{n} \times \vec{E}_{\text{inc}}(\vec{r})$, respectively. The hypersingular part of (3) is handled by transferring the gradient operator ∇' to the testing function [29].

B. The Conventional AIM

In the AIM, a regular grid is superimposed on the bounding box associated with S , and \mathbf{L} is written as

$$\mathbf{L} = \mathbf{L}_{\text{NR}} + \mathbf{L}_{\text{FR}}, \quad (6)$$

where \mathbf{L} represents either $\mathbf{L}^{(A)}$ or $\mathbf{L}^{(\phi)}$. Matrix \mathbf{L}_{NR} is sparse and contains the near-region entries of \mathbf{L} , and is computed

accurately using direct integration. Matrix \mathbf{L}_{FR} contains far-region interactions, which are less dominant and can be approximated as

$$\mathbf{L}_{\text{FR}} \approx \mathbf{W}^{(\text{L})} \mathbf{H}(k_0) \mathbf{P}^{(\text{L})} - \mathbf{L}_{\text{P}}, \quad (7)$$

where matrix $\mathbf{P}^{(\text{L})}$ projects sources from the mesh to the AIM grid, $\mathbf{H}(k_0)$ is the convolution matrix encoding the Green's function, and $\mathbf{W}^{(\text{L})}$ interpolates the computed potentials back onto the mesh. Due to the Toeplitz nature of $\mathbf{H}(k_0)$, matrix-vector products involving \mathbf{L}_{FR} are accelerated with FFTs [23]. The AIM approximation is inaccurate in the near-region due to the singularity of $G(k_0, \vec{r}, \vec{r}')$ when $\vec{r} = \vec{r}'$. Therefore, the precorrection matrix \mathbf{L}_{P} is used to cancel out the contribution of $\mathbf{W}^{(\text{L})} \mathbf{H}(k_0) \mathbf{P}^{(\text{L})}$ in the near region [23],

$$\mathbf{L}_{\text{P}} = \mathbf{W}^{(\text{L})} \mathbf{H}_{\text{NR}}(k_0) \mathbf{P}^{(\text{L})}, \quad (8)$$

where $\mathbf{H}_{\text{NR}}(k_0)$ is the convolution matrix associated with the near region.

Although \mathbf{L}_{NR} is sparse, its assembly with direct integration is still expensive for large problems, particularly when the structure is densely packed and requires a fine mesh to resolve intricate features. This is especially cumbersome for layered background media which require the expensive multilayer Green's function (MGF) [16], which is significantly more expensive to compute than its free space counterpart. Both \mathbf{L}_{NR} and \mathbf{L}_{P} must be generated at each frequency point, which can be a major bottleneck for wideband frequency sweeps.

III. PROPOSED METHOD

The conventional AIM has the following limitation: due to the singularity of the Green's function at $r = 0$, the entries of \mathbf{L}_{NR} cannot be approximated with interpolation, and must instead be computed with direct integration. The singular behavior of $G(k_0, \vec{r}, \vec{r}')$ may be investigated further through a Taylor expansion about $r = 0$,

$$G(k_0, \vec{r}, \vec{r}') = \frac{1}{4\pi r} + \frac{(-jk_0)}{4\pi} + \frac{(-jk_0)^2}{4\pi \cdot 2!} r + \frac{(-jk_0)^3}{4\pi \cdot 3!} r^2 + \dots \quad (9)$$

The first term on the right-hand side of (9) is frequency-independent, and is the static Green's function [35]. The remaining terms on the right-hand side of (9) are frequency-dependent. Therefore, we may write

$$G(k_0, \vec{r}, \vec{r}') = G_{\text{s}}(\vec{r}, \vec{r}') + G_{\text{d}}(k_0, \vec{r}, \vec{r}'), \quad (10)$$

where

$$G_{\text{s}}(\vec{r}, \vec{r}') = \frac{1}{4\pi r} \quad (11)$$

is frequency-independent, and

$$G_{\text{d}}(k_0, \vec{r}, \vec{r}') = G(k_0, \vec{r}, \vec{r}') - G_{\text{s}}(\vec{r}, \vec{r}') = \frac{e^{-jk_0 r} - 1}{4\pi r}. \quad (12)$$

is frequency-dependent. Equations (9) and (10) reveal the key observations underlying the proposed method:

- the singularity of the Green's function is contained entirely in its frequency-independent part, $G_{\text{s}}(\vec{r}, \vec{r}')$;
- since each frequency-dependent term on the right-hand side of (9) is either constant, or decays to 0 as $r \rightarrow 0$, $G_{\text{d}}(k_0, \vec{r}, \vec{r}')$ is a smooth function for any finite r .

This leads to our main hypothesis: $G_{\text{d}}(k_0, \vec{r}, \vec{r}')$ is amenable to approximation by interpolation, even in the near region where r is small. Therefore, \mathbf{L}_{NR} may also be decomposed into frequency-independent and frequency-dependent parts. Then, only the frequency-independent part needs to be computed accurately via direct integration, which does not have to be repeated at each frequency point. Instead, the frequency-dependent part is computed in an accelerated manner with the AIM *even in the near region*, leading to the proposed extended adaptive integral method (AIMx).

A. AIMx for the Single-Layer Potential Operator

Using (10) in (3) allows decomposing the single-layer potential operator \mathcal{L} as

$$\mathcal{L} \left[\vec{X}(\vec{r}') \right] (k_0, \vec{r}) = \mathcal{L}_{\text{s}} \left[\vec{X}(\vec{r}') \right] (\vec{r}) + \mathcal{L}_{\text{d}} \left[\vec{X}(\vec{r}') \right] (k_0, \vec{r}), \quad (13)$$

where the frequency-independent part is

$$\begin{aligned} \mathcal{L}_{\text{s}} \left[\vec{X}(\vec{r}') \right] (\vec{r}) &= \int_{\mathcal{S}} \left(\vec{X}(\vec{r}') + \frac{1}{k_0^2} \nabla' \nabla' \cdot \vec{X}(\vec{r}') \right) G_{\text{s}}(\vec{r}, \vec{r}') d\mathcal{S}, \end{aligned} \quad (14)$$

and the frequency-dependent part is

$$\begin{aligned} \mathcal{L}_{\text{d}} \left[\vec{X}(\vec{r}') \right] (k_0, \vec{r}) &= \int_{\mathcal{S}} \left(\vec{X}(\vec{r}') + \frac{1}{k_0^2} \nabla' \nabla' \cdot \vec{X}(\vec{r}') \right) G_{\text{d}}(k_0, \vec{r}, \vec{r}') d\mathcal{S}. \end{aligned} \quad (15)$$

Correspondingly, \mathbf{L} may be decomposed as

$$\mathbf{L}(k_0) = \mathbf{L}_{\text{s}} + \mathbf{L}_{\text{d}}(k_0), \quad (16)$$

where \mathbf{L}_{s} and $\mathbf{L}_{\text{d}}(k_0)$ represent either the vector or scalar potential parts of the discretized \mathcal{L}_{s} and \mathcal{L}_{d} operators, respectively. The goal is to avoid the explicit assembly of \mathbf{L}_{d} , and to instead directly compute the product of \mathbf{L}_{d} with a vector with the AIM.

To this end, only the frequency-independent matrix \mathbf{L}_{s} is split into near- and far-region contributions as per (6),

$$\mathbf{L}(k_0) = \mathbf{L}_{\text{s, NR}} + \mathbf{L}_{\text{s, FR}} + \mathbf{L}_{\text{d}}(k_0). \quad (17)$$

In (17), the singularity of $G(k_0, \vec{r}, \vec{r}')$ is contained entirely in the sparse, frequency-independent matrix $\mathbf{L}_{\text{s, NR}}$, which is computed accurately with direct integration. The AIM is employed to express the remaining matrices,

$$\begin{aligned} \mathbf{L}_{\text{s, FR}} + \mathbf{L}_{\text{d}}(k_0) &\approx -\mathbf{L}_{\text{s, P}} + \mathbf{W}^{(\text{L})} \mathbf{H}_{\text{s}} \mathbf{P}^{(\text{L})} \\ &\quad + \mathbf{W}^{(\text{L})} \mathbf{H}_{\text{d}}(k_0) \mathbf{P}^{(\text{L})}, \end{aligned} \quad (18)$$

where

$$\mathbf{L}_{\text{s, P}} = \mathbf{W}^{(\text{L})} \mathbf{H}_{\text{s, NR}} \mathbf{P}^{(\text{L})}, \quad (19)$$

is the near-region precorrection matrix associated to $\mathbf{L}_{s, \text{NR}}$, and \mathbf{H}_s and $\mathbf{H}_d(k_0)$ are convolution matrices depending on $G_s(\vec{r}, \vec{r}')$ and $G_d(k_0, \vec{r}, \vec{r}')$, respectively. Matrix $\mathbf{H}_{s, \text{NR}}$ is the convolution matrix for near-region precorrections, and encodes $G_s(\vec{r}, \vec{r}')$. It should be noted that precorrections are required only for $\mathbf{L}_{s, \text{NR}}$, because both near- and far-region contributions of $\mathbf{L}_d(k_0)$ are approximated with the AIM. Since $\mathbf{H}_s + \mathbf{H}_d(k_0) = \mathbf{H}(k_0)$, (18) can be simplified further by combining its last two terms,

$$\mathbf{L}(k_0) \approx \mathbf{L}_{s, \text{NR}} - \mathbf{L}_{s, \text{P}} + \mathbf{W}^{(\mathbf{L})} \mathbf{H}(k_0) \mathbf{P}^{(\mathbf{L})}. \quad (20)$$

Equation (20) is the proposed AIMx matrix decomposition for the single-layer potential operator. Finally, using (20) in (5) yields the AIMx-accelerated EFIE for PECs,

$$-j\omega\mu_0 \left[\mathbf{L}_{s, \text{NR}}^{(A)} - \mathbf{L}_{s, \text{P}}^{(A)} + \mathbf{W}^{(A)} \mathbf{H}(k_0) \mathbf{P}^{(A)} + \frac{1}{k_0} \left(\mathbf{L}_{s, \text{NR}}^{(\phi)} - \mathbf{L}_{s, \text{P}}^{(\phi)} + \mathbf{W}^{(\phi)} \mathbf{H}(k_0) \mathbf{P}^{(\phi)} \right) \right] \mathbf{J} = \mathbf{E}_{\text{inc}}, \quad (21)$$

where the superscript (A) or (ϕ) indicates that the associated matrix corresponds to the vector or scalar potential part of \mathcal{L} , respectively.

In (21), all frequency-dependent effects are approximated with interpolation onto the auxiliary grid, and the associated matrix-vector products are accelerated with FFTs. The key advantage of the proposed method is that the entries of $\mathbf{L}_{s, \text{NR}}^{(A)}$, $\mathbf{L}_{s, \text{NR}}^{(\phi)}$, $\mathbf{L}_{s, \text{P}}^{(A)}$ and $\mathbf{L}_{s, \text{P}}^{(\phi)}$ are frequency-independent, and need only be computed once, enabling significantly faster frequency sweeps compared to the conventional AIM. An important property of the proposed method is its simplicity of implementation. Compared to an existing implementation of the conventional AIM, the proposed method requires only two changes:

- 1) the near-region and precorrection matrices, $\mathbf{L}_{s, \text{NR}}$ and $\mathbf{L}_{s, \text{P}}$, must be assembled using the kernel $G_s(\vec{r}, \vec{r}')$ rather than $G(k_0, \vec{r}, \vec{r}')$;
- 2) a minor modification to \mathbf{H} must be made, which is described in Section III-A1

The fact that direct integration is only required for the frequency-dependent part of (10) was also exploited in [37], where the Taylor expansion (9) is explicitly used to obtain a series of matrices to accurately handle very low frequencies. However, unlike [37], the proposed method does not explicitly use a series expansion, and therefore avoids the need for an increasingly large number of matrix terms at high frequencies. Furthermore, the proposed method is applicable to both the single- and double-layer potential operators [35] for both the free space and the multilayer Green's function. The Taylor expansion of the Green's function has also been used to speed up near-region computations in [38] for free space, and [39], [40] for layered media. However, unlike these methods, the proposed technique does not explicitly utilize a Taylor expansion, and allows the direct integration step to be performed independently of the frequency.

1) *Modification to the Convolution Matrix \mathbf{H}* : Assuming that the AIM grid contains N_g grid points, the (m, n) entry of \mathbf{H} is

$$\mathbf{H}^{(m, n)} = G(k_0, \vec{r}_m, \vec{r}_n), \quad (22)$$

where $m, n = 1, 2, \dots, N_g$, and \vec{r}_i is the i^{th} grid point. Due to the regularity of the AIM grid and the translation-invariance of $G(k_0, \vec{r}, \vec{r}')$, \mathbf{H} is a three-level Toeplitz matrix [23]. Therefore, only its first row contains unique entries which must be computed and stored. When $m = n$, the source and observation grid points coincide, i.e. $r = 0$. The term $\mathbf{H}^{(m, m)}$ is not well defined, since $G(k_0, \vec{r}, \vec{r}') \rightarrow \infty$ as $r \rightarrow 0$. However, the $r = 0$ case necessarily resides within the near region, and is accounted for with direct integration using appropriate singularity subtraction or cancellation techniques [29]. Therefore, in the conventional AIM, one can set $\mathbf{H}^{(m, m)}$ to an arbitrary value, so long as $\mathbf{H}_{\text{NR}}^{(m, m)}$ is set to the same value. This ensures that $\mathbf{H}^{(m, m)}$ is cancelled out when near-region precorrections are applied.

In the proposed AIMx, the $\mathbf{H}^{(m, m)}$ term must be handled more carefully. The contribution of $G_s(\vec{r}, \vec{r}')$ in the near region, particularly when $r = 0$, is accounted for by $\mathbf{L}_{s, \text{NR}}$ via direct integration, with the extraction or cancellation of the singularity [29]. Therefore, $\mathbf{H}_s^{(m, m)}$ can be set to an arbitrary value, so long as $\mathbf{H}_{s, \text{NR}}^{(m, m)}$ is set to the same value. For simplicity, we set

$$\mathbf{H}_s^{(m, m)} = \mathbf{H}_{s, \text{NR}}^{(m, m)} = 0. \quad (23)$$

The term $\mathbf{H}_d^{(m, m)}$ contains the contribution of $G_d(k_0, \vec{r}, \vec{r}')$ for $r = 0$, which must still be accounted for and can be obtained by inspection of (9). The first term on the right-hand side of (9) is $G_s(\vec{r}, \vec{r}')$, while the remaining terms represent $G_d(k_0, \vec{r}, \vec{r}')$,

$$G_d(k_0, \vec{r}, \vec{r}') = \frac{(-jk_0)}{4\pi} + \frac{(-jk_0)^2}{4\pi \cdot 2!} r + \frac{(-jk_0)^3}{4\pi \cdot 3!} r^2 + \dots \quad (24)$$

When $r = 0$, all but the first term on the right-hand side of (24) are 0. Therefore, we let

$$\mathbf{H}_d^{(m, m)} = G_d(k_0, \vec{r}_m, \vec{r}_m) = \frac{(-jk_0)}{4\pi}. \quad (25)$$

Finally, since $\mathbf{H}^{(m, m)} = \mathbf{H}_s^{(m, m)} + \mathbf{H}_d^{(m, m)}$, using (23) and (25) we have

$$\mathbf{H}^{(m, m)} = \mathbf{H}_d^{(m, m)} = \frac{(-jk_0)}{4\pi}, \quad (26)$$

which is the simple modification that must be made to \mathbf{H} compared to the conventional AIM. This modification ensures that there is no undefined behavior when $r = 0$, and that \mathbf{H} correctly accounts for frequency-dependent effects for all values of r , including $r = 0$.

2) *Preconditioning*: The fact that only frequency-independent near-region interactions are precomputed with the MoM has important implications for constructing a preconditioner to solve (21) iteratively. Common choices of preconditioner include diagonal, near-region and block-diagonal entries of \mathbf{L} [41], [42]. The key challenge in

preconditioner assembly for the proposed method is that $\mathbf{L}_d(k_0)$ is not assembled explicitly, and only the entries of \mathbf{L}_s are available prior to the iterative solution of (21).

In the case of diagonal preconditioning, only the self-terms of \mathbf{L} are involved, which are dominated by the contribution of $G_s(\vec{r}, \vec{r}')$. Therefore, it is reasonable to expect that in the proposed method, using the diagonal of \mathbf{L}_s as the preconditioner should be just as effective as using the diagonal of \mathbf{L} , as in the conventional AIM. This is indeed the case, as demonstrated through several numerical examples in Section V.

In the case of near-region or block-diagonal preconditioning, using the entries of \mathbf{L}_s in the proposed AIMx may not be as effective as using those of \mathbf{L} , as in the conventional AIM. This is because the off-diagonal entries of \mathbf{L} become increasingly influenced by $G_d(k_0, \vec{r}, \vec{r}')$ as r increases. If off-diagonal entries of \mathbf{L} are required for preconditioning, one may use FFTs via (20) to explicitly generate selected entries of $\mathbf{L}_d(k_0)$ to augment the corresponding entries of \mathbf{L}_s . This procedure may be performed at each frequency point, or at every few frequency points. The associated computational cost is similar to that of the near-region precorrection phase of the conventional AIM, which may be significant but is not typically a bottleneck. Crucially, the direct integration procedure is still avoided at each new frequency point.

B. AIMx for the Double-Layer Potential Operator

When \mathcal{S} is a closed surface, one may also express $\vec{J}(\vec{r})$ via the magnetic field integral equation (MFIE) [29],

$$-\hat{n} \times \hat{n} \times \mathcal{K} \left[\vec{J}(\vec{r}') \right] (k_0, \vec{r}) = \hat{n} \times \hat{n} \times \vec{H}_{\text{inc}}(\vec{r}), \quad (27)$$

where, in free space, the double-layer potential operator [35] \mathcal{K} is defined as [43]

$$\mathcal{K} \left[\vec{X}(\vec{r}') \right] (k_0, \vec{r}) = \int_{\mathcal{S}} \nabla G(k_0, \vec{r}, \vec{r}') \times \vec{X}(\vec{r}') d\mathcal{S}, \quad (28)$$

where

$$\nabla G(k_0, \vec{r}, \vec{r}') = -\hat{r} (1 + jk_0 r) \frac{e^{-jk_0 r}}{4\pi r^2}, \quad (29)$$

and $\hat{r} = (\vec{r} - \vec{r}')/r$. For closed PEC objects, it is often desirable to formulate an integral equation by adding (2) to a scaled version of (27), to obtain the combined field integral equation (CFIE) [29],

$$-j\omega\mu_0 \hat{n} \times \mathcal{L} \left[\vec{J}(\vec{r}') \right] (k_0, \vec{r}) - \eta_0 \hat{n} \times \hat{n} \times \mathcal{K} \left[\vec{J}(\vec{r}') \right] (k_0, \vec{r}) \\ = \hat{n} \times \vec{E}_{\text{inc}}(\vec{r}) + \eta_0 \hat{n} \times \hat{n} \times \vec{H}_{\text{inc}}(\vec{r}), \quad (30)$$

where η_0 is the wave impedance of free space. Discretizing and testing (30) as before yields its discrete counterpart,

$$[-j\omega\mu_0 \mathbf{L} - \eta_0 \mathbf{K}] \mathbf{J} = \mathbf{E}_{\text{inc}} + \eta_0 \mathbf{H}_{\text{inc}}, \quad (31)$$

where \mathbf{K} is the discretized $\hat{n} \times \hat{n} \times \mathcal{K}$ operator, and column vector \mathbf{H}_{inc} contains coefficients of the basis functions associated with $\hat{n} \times \vec{H}_{\text{inc}}(\vec{r})$.

To develop the proposed method for the \mathcal{K} operator, we expand $\nabla G(k_0, \vec{r}, \vec{r}')$ in a Taylor series about $r = 0$,

$$\nabla G(k_0, \vec{r}, \vec{r}') \\ = -\frac{\hat{r}}{4\pi} \left(\frac{1}{r^2} - \frac{(-jk_0)^2}{2!} - 2\frac{(-jk_0)^3}{3!} r + \dots \right). \quad (32)$$

As in the case of $G(k_0, \vec{r}, \vec{r}')$, the singularity of $\nabla G(k_0, \vec{r}, \vec{r}')$ is contained entirely in the first term on the right-hand side of (32), which is frequency-independent. The remaining frequency-dependent terms are either constant or decay to 0 as $r \rightarrow 0$, and are smooth functions for small r . Following the same approach devised in Section III-A for \mathcal{L} , we may express \mathcal{K} as

$$\mathcal{K} \left[\vec{X}(\vec{r}') \right] (k_0, \vec{r}) = \mathcal{K}_s \left[\vec{X}(\vec{r}') \right] (\vec{r}) + \mathcal{K}_d \left[\vec{X}(\vec{r}') \right] (k_0, \vec{r}), \quad (33)$$

where the frequency-independent part is

$$\mathcal{K}_s \left[\vec{X}(\vec{r}') \right] (\vec{r}) = \int_{\mathcal{S}} \nabla G_s(\vec{r}, \vec{r}') \times \vec{X}(\vec{r}') d\mathcal{S}, \quad (34)$$

and the frequency-dependent part is

$$\mathcal{K}_d \left[\vec{X}(\vec{r}') \right] (k_0, \vec{r}) = \int_{\mathcal{S}} \nabla G_d(k_0, \vec{r}, \vec{r}') \times \vec{X}(\vec{r}') d\mathcal{S}, \quad (35)$$

In (34) and (35),

$$\nabla G_s(\vec{r}, \vec{r}') = -\frac{\hat{r}}{4\pi r^2}, \quad (36)$$

and

$$\nabla G_d(k_0, \vec{r}, \vec{r}') = \nabla G(k_0, \vec{r}, \vec{r}') - \nabla G_s(\vec{r}, \vec{r}'). \quad (37)$$

Therefore, \mathbf{K} may be decomposed as

$$\mathbf{K}(k_0) = \mathbf{K}_s + \mathbf{K}_d(k_0), \quad (38)$$

where \mathbf{K}_s and $\mathbf{K}_d(k_0)$ are the discretized \mathcal{K}_s and \mathcal{K}_d operators, respectively.

Following the approach in Section III-A, \mathbf{K} may be approximated as

$$\mathbf{K} \approx \mathbf{K}_{s,\text{NR}} - \mathbf{K}_{s,\text{P}} + \mathbf{W}^{(\mathbf{K})} \mathbf{H}_{\nabla} \mathbf{P}^{(\mathbf{K})}, \quad (39)$$

where $\mathbf{K}_{s,\text{NR}}$ and $\mathbf{K}_{s,\text{P}}$ are the near-region and precorrection matrices, respectively, which are frequency-independent and involve the kernel $\nabla G_s(\vec{r}, \vec{r}')$, and \mathbf{H}_{∇} is the convolution matrix encoding $\nabla G(k_0, \vec{r}, \vec{r}')$. Matrices $\mathbf{W}^{(\mathbf{K})}$ and $\mathbf{P}^{(\mathbf{K})}$ are the interpolation and projection matrices associated with \mathbf{K} , respectively. In keeping with the discussion in Section III-A1, the self-term of \mathbf{H}_{∇} should be set as

$$\mathbf{H}_{\nabla}^{(0,0)} = \nabla G_d(k_0, \vec{r}_0, \vec{r}_0) = \frac{(-jk_0)^2}{4\pi \cdot 2!}, \quad (40)$$

which is the second term of the expansion (32). The singularity of $\nabla G_s(\vec{r}, \vec{r}')$ at $r = 0$ is accounted for with direct integration via $\mathbf{K}_{s,\text{NR}}$.

Finally, using (20) and (39) in (31), we obtain the AIMx-accelerated CFIE for PECs,

$$\begin{aligned}
 & -j\omega\mu_0 \left[\left(\mathbf{L}_{s,\text{NR}}^{(A)} - \mathbf{L}_{s,\text{P}}^{(A)} + \mathbf{W}^{(A)} \mathbf{H} \mathbf{P}^{(A)} \right) \right. \\
 & \quad \left. + \frac{1}{k_0^2} \left(\mathbf{L}_{s,\text{NR}}^{(\phi)} - \mathbf{L}_{s,\text{P}}^{(\phi)} + \mathbf{W}^{(\phi)} \mathbf{H} \mathbf{P}^{(\phi)} \right) \right. \\
 & \quad \left. - \frac{j}{k_0} \left(\mathbf{K}_{s,\text{NR}} - \mathbf{K}_{s,\text{P}} + \mathbf{W}^{(\mathbf{K})} \mathbf{H}_{\nabla} \mathbf{P}^{(\mathbf{K})} \right) \right] \mathbf{J} \\
 & = \mathbf{E}_{\text{inc}} + \eta_0 \mathbf{H}_{\text{inc}}. \quad (41)
 \end{aligned}$$

The comments regarding preconditioners in Section III-A2 apply to (41) as well.

C. AIMx for Layered Background Media

For layered background media, we consider the multilayer Green's function (MGF) as described in formulation C of [44], though the proposed method may be extended to other formulations as well. The definition of \mathcal{L} becomes [43]

$$\begin{aligned}
 \mathcal{L} \left[\vec{X}(\vec{r}') \right] (\vec{r}) &= \int_S \overline{\overline{\mathbf{G}}}_A(k_0, \vec{r}, \vec{r}') \cdot \vec{X}(\vec{r}') dS \\
 &+ \frac{1}{k_0^2} \int_S \nabla' \nabla' \cdot \vec{X}(\vec{r}') G_\phi(k_0, \vec{r}, \vec{r}') dS, \quad (42)
 \end{aligned}$$

where $\overline{\overline{\mathbf{G}}}_A(k_0, \vec{r}, \vec{r}')$ and $G_\phi(k_0, \vec{r}, \vec{r}')$ are the dyadic and scalar potential Green's functions of the background medium, respectively. The term $G_\phi(k_0, \vec{r}, \vec{r}')$ and the non-zero components of $\overline{\overline{\mathbf{G}}}_A(k_0, \vec{r}, \vec{r}')$ are expressed in terms of semi-infinite integrals in the complex plane, which are known as ‘‘Sommerfeld integrals’’ [16], [45]. These integrals are expensive to compute, even when approximations such as the discrete complex image method (DCIM) [46] are employed. As a result, the near-region computations involving direct integration are particularly time consuming for layered media.

In the following, it is assumed that $G(k_0, \vec{r}, \vec{r}')$ represents either $G_\phi(k_0, \vec{r}, \vec{r}')$, or a non-zero component of $\overline{\overline{\mathbf{G}}}_A(k_0, \vec{r}, \vec{r}')$. Regardless of the method used to compute $G(k_0, \vec{r}, \vec{r}')$, it is common practice to extract the quasistatic contributions in the spectral domain, which are then added back analytically in spatial domain [45]–[47]. This ensures that the integrands involved in the computation of $G(k_0, \vec{r}, \vec{r}')$ decay sufficiently fast [47]. Extracting quasistatic terms also provides a simple way to compute the frequency-independent part of $G(k_0, \vec{r}, \vec{r}')$, as discussed below. Therefore, we may write

$$G(k_0, \vec{r}, \vec{r}') = G_q(k_0, \vec{r}, \vec{r}') + G_r(k_0, \vec{r}, \vec{r}'), \quad (43)$$

where $G_q(k_0, \vec{r}, \vec{r}')$ is the quasistatic part of $G(k_0, \vec{r}, \vec{r}')$, and $G_r(k_0, \vec{r}, \vec{r}')$ is the remainder. In general, $G_q(k_0, \vec{r}, \vec{r}')$ may be expressed as [47]

$$G_q(k_0, \vec{r}, \vec{r}') = \sum_{n=1}^{N_s} G_{sn}(\vec{r}, \vec{r}') + \sum_{n=1}^{N_q} G_{qn}(k_0, \vec{r}, \vec{r}'), \quad (44)$$

where N_s , N_q and the forms of $G_{sn}(\vec{r}, \vec{r}')$ and $G_{qn}(k_0, \vec{r}, \vec{r}')$ all depend on the location of source and observation points [47]. In (44), $G_q(k_0, \vec{r}, \vec{r}')$ contains some terms,

$G_{sn}(\vec{r}, \vec{r}')$, that are already frequency-independent. The other terms, $G_{qn}(k_0, \vec{r}, \vec{r}')$, depend on frequency, and have the form [47],

$$G_{qn}(k_0, \vec{r}, \vec{r}') = \frac{C_n e^{-jk_i \alpha_n}}{4\pi \alpha_n}, \quad (45)$$

where C_n is a constant which depends on the material parameters of the layered medium [47], k_i is the wave number in the layer in which the source resides,

$$\rho = \sqrt{(x-x')^2 + (y-y')^2}, \quad (46)$$

and

$$\alpha_n = \sqrt{\rho^2 + \gamma_n^2}. \quad (47)$$

Term γ_n is a linear function of z , z' and the elevation of source and observation layers [47]. Equation (45) has a form similar to (4), and the Taylor expansion of $G_{qn}(k_0, \vec{r}, \vec{r}')$ about $\alpha = 0$ reads

$$\begin{aligned}
 G_{qn}(k_0, \vec{r}, \vec{r}') &= C_n \left[\frac{1}{4\pi \alpha_n} + \frac{(-jk_i)}{4\pi} \right. \\
 &\quad \left. + \frac{(-jk_i)^2}{4\pi \cdot 2!} \alpha_n + \frac{(-jk_i)^3}{4\pi \cdot 3!} \alpha_n^2 + \dots \right], \quad (48)
 \end{aligned}$$

where again the singularity is contained in the first term, which is frequency-independent. We may decompose $G_{qn}(k_0, \vec{r}, \vec{r}')$ into frequency-independent and frequency-dependent parts as

$$G_{qn}(k_0, \vec{r}, \vec{r}') = \underbrace{\frac{C_n}{4\pi \alpha_n}}_{G_{qsn}(\vec{r}, \vec{r}')} + \underbrace{\frac{C_n}{4\pi} \left(\frac{e^{-jk_i \alpha_n}}{\alpha_n} - \frac{1}{\alpha_n} \right)}_{G_{qdn}(k_0, \vec{r}, \vec{r}')}. \quad (49)$$

Using (49) and (44) in (43), we get

$$\begin{aligned}
 G(k_0, \vec{r}, \vec{r}') &= \sum_{n=1}^{N_s} G_{sn}(\vec{r}, \vec{r}') + \sum_{n=1}^{N_q} G_{qsn}(\vec{r}, \vec{r}') \\
 &+ \sum_{n=1}^{N_q} G_{qdn}(k_0, \vec{r}, \vec{r}') + G_r(k_0, \vec{r}, \vec{r}'), \quad (50)
 \end{aligned}$$

where the first two terms on the right-hand side are frequency-independent and can be denoted as $G_s(\vec{r}, \vec{r}')$, while the last two terms are frequency-dependent and are denoted as $G_d(k_0, \vec{r}, \vec{r}')$. Therefore, (50) may be simplified as

$$G(k_0, \vec{r}, \vec{r}') = G_s(\vec{r}, \vec{r}') + G_d(k_0, \vec{r}, \vec{r}'), \quad (51)$$

which resembles the free space case in (10). This expression holds for both $G_\phi(k_0, \vec{r}, \vec{r}')$ and any non-zero component of $\overline{\overline{\mathbf{G}}}_A(k_0, \vec{r}, \vec{r}')$. Equation (51) indicates that the main ideas of the proposed method also apply to layered media:

- the singular behavior of $G(k_0, \vec{r}, \vec{r}')$ is entirely contained in the frequency-independent term $G_s(\vec{r}, \vec{r}')$;
- the frequency-dependent term $G_d(k_0, \vec{r}, \vec{r}')$ is smooth, and decays to 0 as $r \rightarrow 0$ [45], [47], therefore can be approximated by interpolation even in the near region.

When the quasistatic part of the MGF is expressed as per formulation C in [44], C_n may depend on the complex permittivity of the associated layer, which is frequency-dependent if

the layer is lossy. As a result, for lossy layers, $G_{\text{qs}n}(\vec{r}, \vec{r}')$ may no longer be frequency-independent. A complete treatment of the lossy case is beyond the scope of this paper, and will be the subject of a future publication. In this work, we assume that the layers are either lossless, or that their losses are small enough that the imaginary part of the complex permittivity can be neglected when (45) is evaluated in the near region. As shown in the numerical example in Section V-E, this approximation still yields accurate results for realistic structures of practical importance.

The AIMx concept may also be extended to the curl of $\vec{\mathbf{G}}_A(k_0, \vec{r}, \vec{r}')$ in order to handle the \mathcal{K} operator for layered media [43]. The proposed AIMx-based EFIE, (21), and CFIE, (41), can therefore be applied for PEC objects embedded in layered media. An important advantage of the proposed method for layered media is that the near-region matrix entries are extremely simple to compute, by taking the static limit of $G_q(k_0, \vec{r}, \vec{r}')$. These entries do not require computing Sommerfeld integrals, nor do they require applying approximations such as the DCIM. Therefore, the near-region computations in the proposed method are significantly more efficient, robust, and easy to implement, compared to the conventional AIM.

IV. ERROR ANALYSIS

The proposed method rests on the hypothesis that the frequency-dependent part of the kernels of \mathcal{L} and \mathcal{K} can be approximated with interpolation in both the near and far regions. In this section, this hypothesis is validated for each type of kernel considered, through analytical and numerical error analysis.

We consider the moment-matching version of the AIM [48], which relies on the interpolation of the kernel with polynomials [23]. We use Lagrange polynomials due to their straightforward implementation and the availability of an error bound. Without loss of generality, we can assume that the source is at the origin, so that $\vec{r}' = 0$, and $r = |\vec{r}|$. In addition, we normalize any physical length, say r , as $\theta_r \triangleq k_0 r$.

A. Free Space

We first consider the free space case, and assume that $K(\theta_r)$ can represent either $G_d(\theta_r)$ or $\nabla G_d(\theta_r)$. Consider a regular AIM grid with a stencil which has $n + 1$ points in each direction. Given $n + 1$ samples,

$$(r_0, K(\theta_{r_0})), (r_1, K(\theta_{r_1})) \dots (r_n, K(\theta_{r_n})), \quad (52)$$

the Lagrange polynomial approximation of $K(\theta_r)$ can be written as [49]

$$\tilde{K}_n(\theta_r) = \sum_{q=0}^n K(\theta_{r_q}) \left(\prod_{\substack{m \neq q \\ 0 \leq m \leq n}} \frac{r - r_m}{r_q - r_m} \right). \quad (53)$$

The order n interpolation error is

$$\Delta K_n(\theta_r) = \left| K(\theta_r) - \tilde{K}_n(\theta_r) \right|. \quad (54)$$

The goal is to show that $\Delta K_n(\theta_r)$ is bounded even when $\theta_r \rightarrow 0$, and is controllable via grid refinement.

Following the approach in [50], $\Delta K_n(\theta_r)$ can be bound as [49]

$$\frac{\Delta K_n(\theta_r)}{k_0} \leq \underbrace{\frac{(\theta_{r_n} - \theta_{r_0})^{n+1}}{(n+1)!} \max_{\theta_{r_0} \leq \theta_\xi \leq \theta_{r_n}} \left| \frac{d^{(n+1)}}{d\theta_\xi^{(n+1)}} [K(\theta_\xi)] \right|}_{B_n(\theta_r)}, \quad (55)$$

where θ_{r_0} and θ_{r_n} are the stencil coordinates nearest to and farthest from the source point, respectively. When $K(\theta_r) = G_d(\theta_r)$,

$$\begin{aligned} \frac{d^{(n+1)}}{d\theta_\xi^{(n+1)}} [K(\theta_\xi)] &= \frac{(-1)^{n+1}}{4\pi\theta_\xi^{n+2}} (n+1)! \cdot \\ &\left[-1 + \sum_{l=0}^{n+1} \binom{n+1}{l} \frac{(n+1-l)!}{(n+1)!} (-j\theta_\xi)^l e^{-j\theta_\xi} \right], \end{aligned} \quad (56)$$

and when $K(\theta_r) = \nabla G_d(\theta_r)$,

$$\begin{aligned} \frac{d^{(n+1)}}{d\theta_\xi^{(n+1)}} [K(\theta_\xi)] &= \frac{-\hat{\theta}}{4\pi} \sum_{l=0}^{n+1} \binom{n+1}{l} \frac{(-n-2+l)_{(n+1-l)}}{\theta_\xi^{n+3-l}} \cdot \\ &[-\delta_l + (-j)^l e^{-j\theta_\xi} (1 + j\theta_\xi - l)]. \end{aligned} \quad (57)$$

In (57), $\hat{\theta} = k_0 \hat{r}$, the notation $(a)_{(b)}$ indicates the rising factorial (“Pochhammer function”) [49], and

$$\delta_l = \begin{cases} 1 & \text{if } l = 0, \\ 0 & \text{otherwise.} \end{cases} \quad (58)$$

When $\theta_r = 0$, (56) and (57) cannot be evaluated numerically due to their indeterminate forms. Instead, one can evaluate $\lim_{\theta_r \rightarrow 0} B_n(\theta_r)$ by recursively applying the L’Hôpital rule, or by using symbolic math software [51], to get

$$\lim_{\theta_r \rightarrow 0} B_n(\theta_r) = \frac{(\theta_{r_n} - \theta_{r_0})^{n+1}}{(n+1)!} \left(\frac{1}{n+2} \right) \quad (59)$$

for $K(\theta_r) = G_d(\theta_r)$, and

$$\lim_{\theta_r \rightarrow 0} B_n(\theta_r) = \frac{(\theta_{r_n} - \theta_{r_0})^{n+1}}{(n+1)!} \left(\frac{1}{n+3} \right) \quad (60)$$

for $K(\theta_r) = \nabla G_d(\theta_r)$. In both cases, $\lim_{\theta_r \rightarrow 0} B_n(\theta_r)$ is a constant, which confirms that the Lagrange interpolation error for both $G_d(\theta_r)$ and $\nabla G_d(\theta_r)$ is bounded even for $\theta_r = 0$.

Fig. 1 shows, over a wide range of electrical sizes, the results of the error analysis for $G_d(\theta_r)$, for $n = 2$. Fig. 2 shows the same for $\nabla G_d(\theta_r)$. In both cases, the top panel shows the exact and interpolated curves, for the given sample points indicated with vertical black bars. It is assumed that 10 samples are used per wavelength. The magenta dashed line shows a typical choice for the size of the near region. The bottom panel shows the computed numerical error, as well as the analytical bound $B_n(\theta_r)$. The green dashed line indicates the value of $\lim_{\theta_r \rightarrow 0} B_n(\theta_r)$ obtained from (59) and (60). Fig. 1 and Fig. 2 clearly indicate that the error is bounded as $\theta_r \rightarrow 0$, and is not significantly larger within the near region, as compared to the region just beyond. Also plotted in the bottom panel is the computed numerical error when the number of samples is increased to 20 and 30 points per

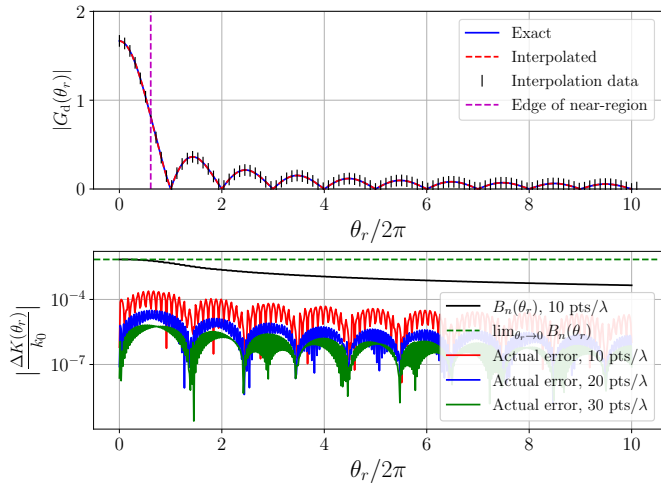


Fig. 1: Top panel: Lagrange interpolation of $G_d(\theta_r)$ for $n = 2$. Bottom panel: computed numerical error, and $B_n(\theta_r)$ computed via (56).

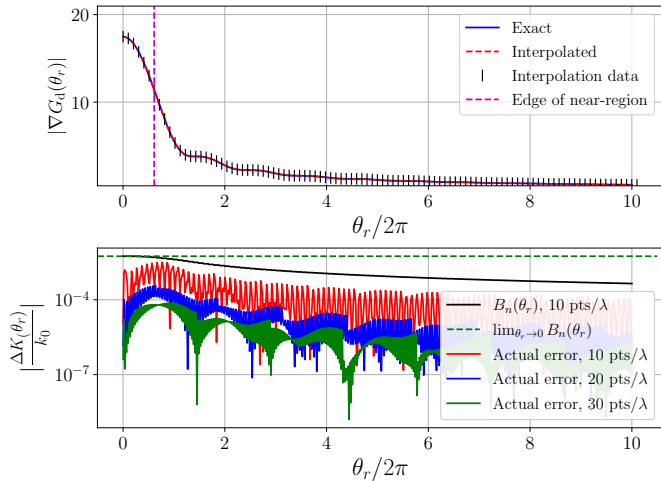


Fig. 2: Top panel: Lagrange interpolation of $\nabla G_d(\theta_r)$ for $n = 2$. Bottom panel: computed numerical error, and $B_n(\theta_r)$ computed via (57).

wavelength, confirming that the error is controllable via grid refinement. Therefore, the frequency-dependent part of the free space Green's function and its gradient can be interpolated with polynomials for all θ_r , including the near region.

B. Layered Media

Deriving an analytical bound from (55) for layered media is more challenging due to the many possible forms that individual dyadic components assume. Instead, we compute the bounds by evaluating the derivative in (55) with a finite difference approximation for some representative examples. Table I shows the dielectric layer configuration used for the error analysis in this section, and it is assumed that $z = z' = 0.4$ mm, where $z = 0$ is taken as the interface between the lowermost layer and the PEC backing. Fig. 3 shows the Lagrange interpolation and associated error where $K(\theta_r)$

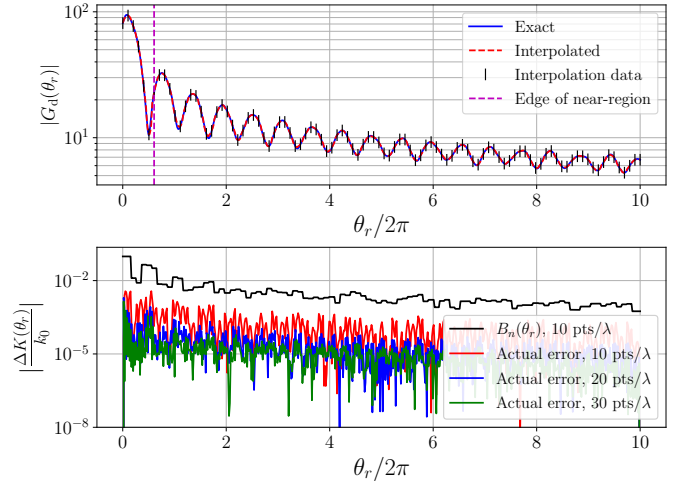


Fig. 3: Top panel: Lagrange interpolation of the frequency-dependent part of $\overline{G}_A(k_0, \vec{r}, \vec{r}')$, for the xx component, for $n = 2$. Bottom panel: computed numerical error, and $B_n(\theta_r)$ computed via finite difference-based evaluation of (55).

TABLE I: Dielectric layer configurations for the error analysis in Section IV-B and the numerical examples in Section V. Layers are non-magnetic, and h represents their height.

Error Analysis (Section IV-B)		Dipole Array (Section V-D)		Inductor Array (Section V-E)	
ϵ_r	h (mm)	ϵ_r	h (mm)	ϵ_r	σ (S/m) h (μ m)
Air	∞	Air	∞	Air	∞
2.1	0.7			2.1	0 6
12.5	0.3			3.7	0 11
9.8	0.5	2.17	0.254	2.1	0 12
8.6	0.3	1.04	5.77	3.7	0 11
				9.0	0 25
				11.9	10 20
PEC	∞	PEC	∞	PEC	∞

is taken as the xx component of the frequency-dependent part of $\overline{G}_A(k_0, \vec{r}, \vec{r}')$. As in the free space case, the error remains bounded as $\theta_r \rightarrow 0$, and is not significantly larger inside the near region than just outside. Furthermore, the error can be controlled via grid refinement. Therefore, the idea of interpolating dynamic contributions of the kernel in both near and far regions extends to the modeling of layered media with the MGF.

V. RESULTS

The accuracy and efficiency of the proposed method are demonstrated in this section, through comparisons with the conventional AIM. All simulations were performed single-threaded on a 3 GHz Intel Xeon CPU. We used PETSc [52] for sparse matrix manipulation. The GMRES iterative solver [53] available through PETSc was used for solving (21) and (41). A relative residual norm of 10^{-4} was used as the GMRES convergence tolerance.

TABLE II: Performance comparison for the numerical examples in Section V.

	Sphere (Section V-A)		NASA Almond (Section V-B)		Reflectarray (Section V-C)		Dipole Array (Section V-D)		Inductor Array (Section V-E)	
	AIM	AIMx	AIM	AIMx	AIM	AIMx	AIM	AIMx	AIM	AIMx
Number of mesh elements	3,080		40,194		254,736		25,042		42,396	
One-time static matrix-fill	--	2.7 sec	--	1.4 min	--	0.5 hr	--	2.2 min	--	0.2 hr
Per-frequency matrix-fill*	3.9 sec	--	1.4 min	--	1.4 hr	--	3.5 min	--	0.3 hr	--
Total CPU time	34.5 min	11.8 min	515.6 min	117.5 min	120.1 hr	7.5 hr	23.5 hr	7.1 hr	24.2 hr	3.5 hr
Overall speed-up	2.9×		4.4×		16.1×		3.3×		6.9×	

*averaged across all frequency points

A. Sphere

We first consider a PEC sphere with diameter 1 m in free space. The sphere is meshed with 3,080 triangles and 4,620 edges, and an AIM grid with $25 \times 25 \times 25$ points along x , y and z , respectively, was used with $n = 2$. A plane wave with the electric field polarized along the y axis is incident on the sphere, and the EFIE system (21) was solved with a diagonal preconditioner. The geometry and computed electric surface current density at 750 MHz are shown in Fig. 4. The top panel of Fig. 5 shows the monostatic radar cross section (RCS) across a range of frequencies computed via the proposed method, compared to the conventional AIM and the analytical Mie series. Excellent agreement between the three methods is observed across the entire frequency range. The bottom panel of Fig. 5 shows the bistatic RCS for the $\phi = 0$ cut, for the low (10 MHz) and high (750 MHz) ends of the considered frequency range. Again, the proposed method agrees perfectly with the conventional AIM.

The top panel of Fig. 6 shows that the proposed method requires the same number of iterations as the conventional AIM except at two frequency points, which are near internal resonances. Therefore, the frequency-independent diagonal preconditioner discussed in Section III-A2 is nearly as effective as the full-wave diagonal preconditioner across the entire frequency range. The bottom panel of Fig. 6 shows the CPU time per frequency, and demonstrates the time saved by avoiding the near-region direct integration and precorrection steps at each frequency. The time taken for near-region computations in both AIMx and the conventional AIM is reported in Table II, and a total speed-up of $2.9\times$ was observed.

B. NASA Almond

Next, we consider the NASA almond [54] in free space, meshed with 26,796 triangles and 40,194 edges. An AIM grid with $126 \times 50 \times 17$ points was used with $n = 2$. A plane wave with the electric field polarized along the x axis is incident on the PEC structure, and the CFIE system (41) was solved with a diagonal preconditioner. The geometry and computed electric surface current density at 10 GHz are shown in Fig. 7. The top pane of Fig. 8 shows the monostatic RCS across a range of frequencies computed via AIMx, compared to the conventional AIM. Excellent agreement is observed across the entire frequency range. The bottom panel of Fig. 8 shows the bistatic RCS for the $\phi = 0$ cut, at 1 GHz and 10 GHz. Again, the proposed method is in excellent agreement with the conventional AIM.

The top panel of Fig. 9 shows that the proposed method requires the same number of iterations to converge as the conventional AIM across the entire frequency range, which reaffirms the effectiveness of the frequency-independent diagonal preconditioner compared to the full-wave version. The bottom panel of Fig. 9 shows the CPU time per frequency, and shows a significant reduction in the computational cost compared to the conventional AIM. The proposed method provided a total speed-up of $4.4\times$, and CPU times are reported in Table II.

C. Planar Reflectarray

We next consider a more realistic test case, involving a four-layer reflectarray in free space with 21×21 planar PEC Jerusalem cross elements. Details regarding the geometry of individual elements can be found in [55], [56]. The array is meshed with 254,736 triangles and 324,420 edges, and an AIM grid with $158 \times 158 \times 7$ points was used with $n = 3$. A plane wave with the electric field polarized along x impinges on the array. To robustly handle the intricate sub-wavelength features of the structure, the augmented EFIE (AEFIE) [7] was used, which involves the same matrix operators as the EFIE (5), but takes the charge density as an additional unknown. The constraint preconditioner [7] involving self-terms of $\mathbf{L}_{s, NR}^{(A)}$ and $\mathbf{L}_{s, NR}^{(\phi)}$ was used. The geometry and computed electric surface current density at 25 GHz are shown in Fig. 10. The monostatic RCS for frequencies from 15 to 25 GHz is shown in the top panel of Fig. 11, which corresponds to electrical sizes from 3.9 to 6.6 wavelengths. Additionally, the directivity for the $\phi = 0$ cut is shown in the bottom panel of Fig. 11 for 15, 20 and 25 GHz. The RCS and directivity computed via the proposed method are both in excellent agreement with results from the conventional AIM.

The top panel of Fig. 12 shows that once again, the preconditioner based on frequency-independent self-terms of $\mathbf{L}_{NR}^{(A)}$ and $\mathbf{L}_{NR}^{(\phi)}$ is just as effective as the full-wave preconditioner proposed in [7] across the entire frequency range considered. Furthermore, the bottom panel of Fig. 12 shows the significantly improved efficiency of the proposed method compared to the conventional AIM. At the lower end of the frequency range, fewer iterations are required in the iterative solve step, and the CPU time in the conventional AIM is dominated by the near-region direct integration and precorrection steps. Instead, at higher frequencies, the number of iterations required to converge increases, showing a commensurate increase in total CPU time in the proposed method, as shown in the bottom

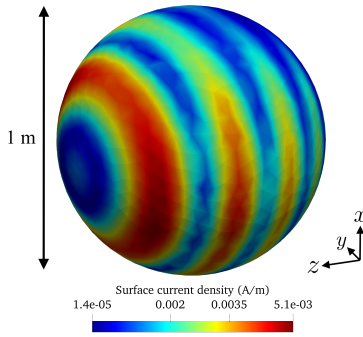


Fig. 4: Geometry and electric surface current density at 750 MHz for the sphere in Section V-A.

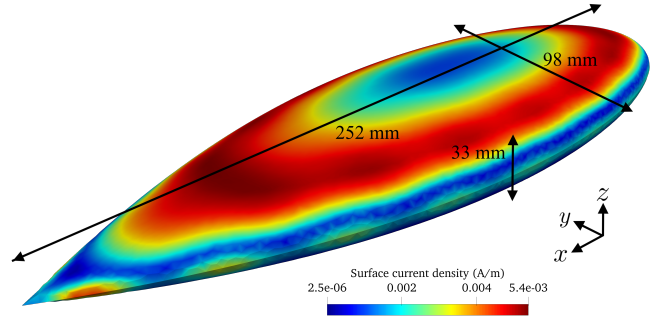


Fig. 7: Geometry and electric surface current density at 10 GHz for the NASA almond in Section V-B.

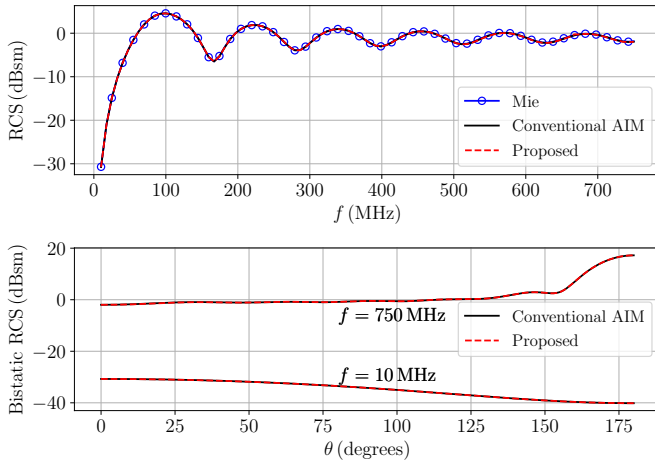


Fig. 5: Accuracy validation for the sphere in Section V-A. Top panel: monostatic RCS. Bottom panel: bistatic RCS at 10 MHz and 750 MHz.

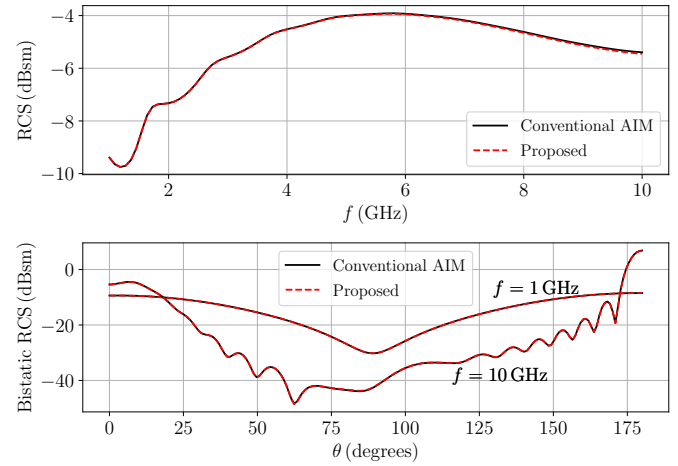


Fig. 8: Accuracy validation for the NASA almond in Section V-B. Top panel: monostatic RCS. Bottom panel: bistatic RCS at 1 GHz and 10 GHz.

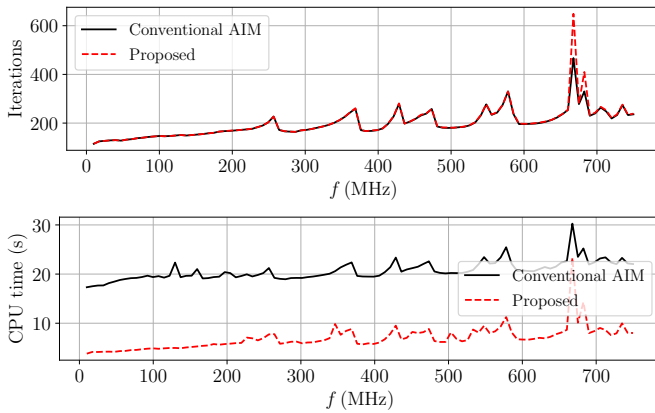


Fig. 6: Performance comparison for the sphere in Section V-A. Top panel: iterations required for convergence. Bottom panel: CPU time per frequency.

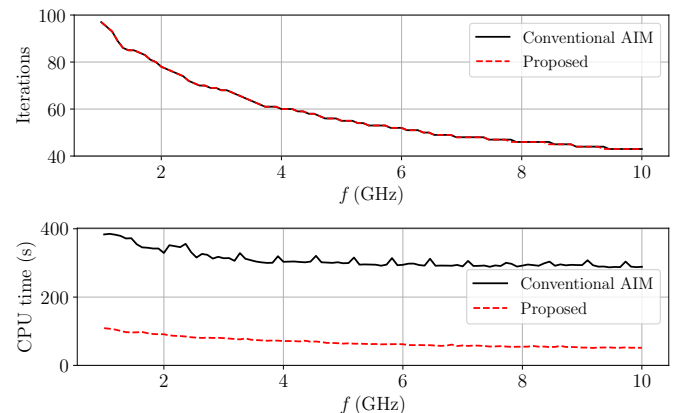


Fig. 9: Performance comparison for the NASA almond in Section V-B. Top panel: iterations required for convergence. Bottom panel: CPU time per frequency.

panel of Fig. 12. However, the overall cost of the conventional AIM is still dominated by the near-region computations. The CPU times for both methods are reported in Table II. It is important to note that besides the per-frequency time savings, the near-region direct integration step in the proposed method

is nearly $3\times$ faster than in the conventional AIM. This is because the static Green's function, $1/(4\pi r)$, is used as the kernel for near-region computations in the proposed method, which is faster to compute than the exponential function in the full-wave Green's function (4), as required in the conventional

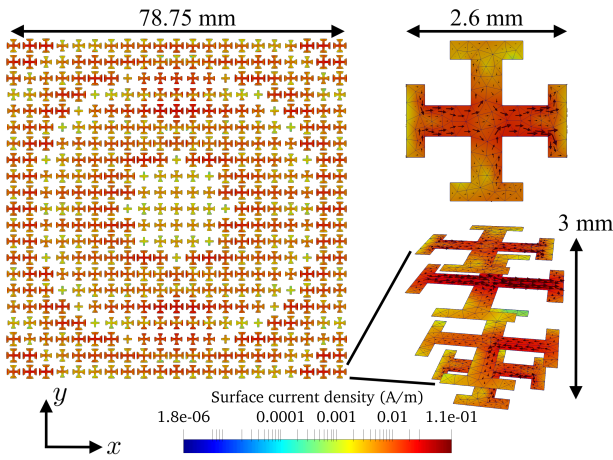


Fig. 10: Geometry and electric surface current density at 25 GHz for the reflectarray in Section V-C.

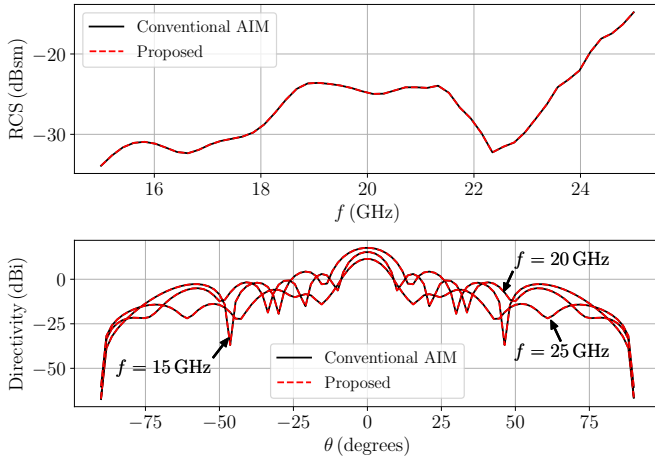


Fig. 11: Accuracy validation for the reflectarray in Section V-C. Top panel: monostatic RCS. Bottom panel: directivity at 15 GHz, 20 GHz and 25 GHz.

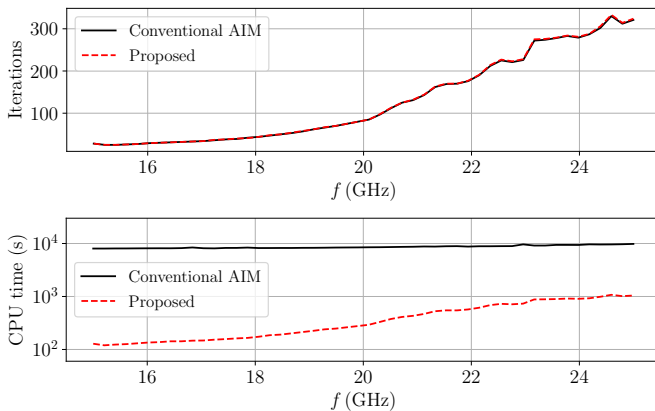


Fig. 12: Performance comparison for the reflectarray in Section V-C. Top panel: iterations required for convergence. Bottom panel: CPU time per frequency.

AIM. The proposed method reduces the total simulation time from over 5 days to just 7.5 hours, which corresponds to an

overall speed-up of $16.1\times$.

D. Printed Dipole Array

The numerical examples considered so far involved structures in free space; the following examples concern structures embedded in layered media. First, we consider a double-sided printed dipole array consisting of planar PEC elements fed by a balanced transmission line network. The structure is shown in Fig. 13, and was inspired by [57], which includes details of the geometry. Each arm of the dipole elements is printed on opposite sides of a dielectric substrate with relative permittivity 2.17, adjacent to a foam spacer backed by a ground plane. The background medium configuration is shown in Table I. The structure is meshed with 25,042 triangles and 33,688 edges, and an AIM grid with $177 \times 177 \times 4$ points was used with $n = 3$. The AEFIE formulation with the same constraint preconditioner as in Section V-C was used, which now involves $G_\phi(k_0, \vec{r}, \vec{r}')$ and $\overline{\mathbf{G}}_A(k_0, \vec{r}, \vec{r}')$ as kernels due to the layered background medium. A delta-gap port [29] was employed to excite the structure, with the port location marked in Fig. 13, which also shows the computed electric surface current density at 20 GHz. Frequencies from 1 to 20 GHz were considered, over which the structure spans electrical sizes between 0.4 and 8 wavelengths. The magnitude and phase of the scattering parameter S_{11} are shown in the top and bottom panels of Fig. 14, respectively. In both cases, the proposed method is in excellent agreement with the conventional AIM over the entire frequency range. This demonstrates that the proposed method is also capable of accurately handling electrically large problems where the MGF is used to model layered background media. The top panel of Fig. 15 again demonstrates the relative efficacy of the constraint preconditioner involving only frequency-independent self-term entries, while the bottom panel of Fig. 15 shows the per-frequency CPU time improvement of the proposed method over the conventional AIM. Table II reports CPU times for the two methods, and shows that the near-region direct integration step in the proposed method is significantly faster than in the conventional AIM. A total speed-up of $3.3\times$ was obtained with the proposed method. In this case, the iterative solve time is a significant contributor to the total simulation time at each frequency, and is the limiting factor in the obtained speed-up.

E. Stacked Inductor Array

As a final example, we consider an on-chip stacked inductor array [3] consisting of $3 \times 4 \times 2$ copper coils, shown in Fig. 16. Each individual element is a $4\times$ scaled version of the geometry described in [58]. The structure is embedded in a six-layer substrate with the configuration shown in Table I. The first inductor layer starts at $z = 45 \mu\text{m}$, and the second at $z = 68 \mu\text{m}$, where $z = 0$ is taken at the interface between the lowermost layer and the PEC backing. A mesh with 42,396 triangles and 63,594 edges was generated, and an AIM grid with $96 \times 100 \times 6$ points was used with $n = 2$. The AEFIE formulation with the same constraint preconditioner as in the previous two examples was used, and the presence of skin effect was modeled with the surface impedance boundary

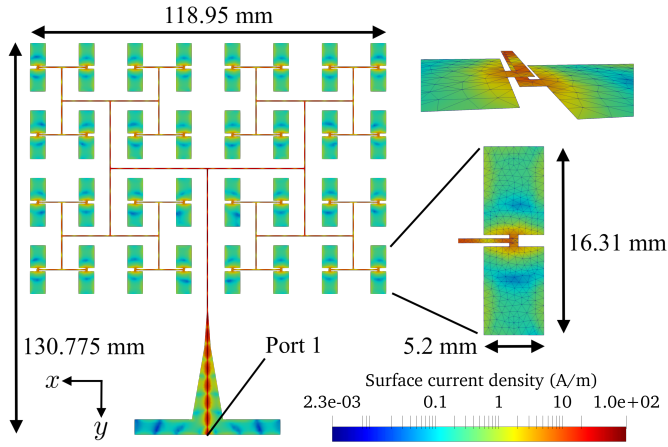


Fig. 13: Geometry and electric surface current density at 20 GHz for the dipole array in Section V-D.

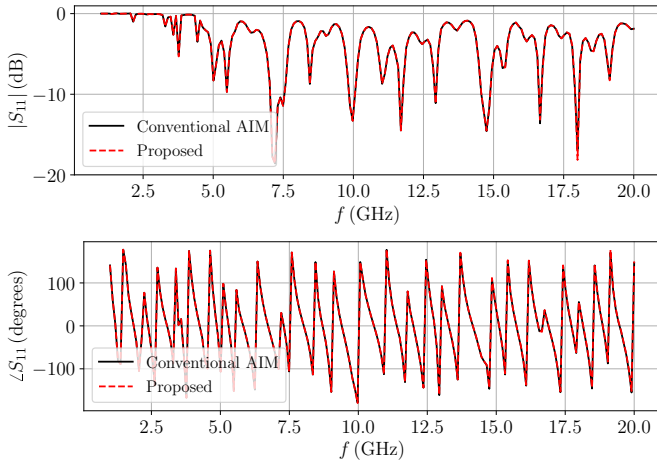


Fig. 14: Accuracy validation for the dipole array in Section V-D. Top panel: magnitude of S_{11} . Bottom panel: phase of S_{11} .

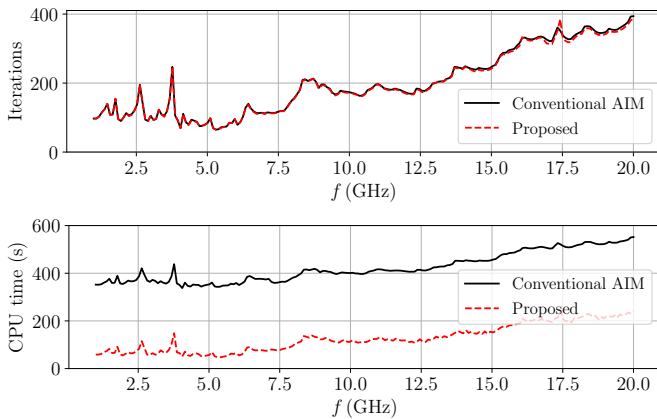


Fig. 15: Performance comparison for the dipole array in Section V-D. Top panel: iterations required for convergence. Bottom panel: CPU time per frequency.

condition (SIBC) [59]. The MGF involving $G_\phi(k_0, \vec{r}, \vec{r}')$ and $\vec{\mathbf{G}}_A(k_0, \vec{r}, \vec{r}')$ was used to model the background medium. A

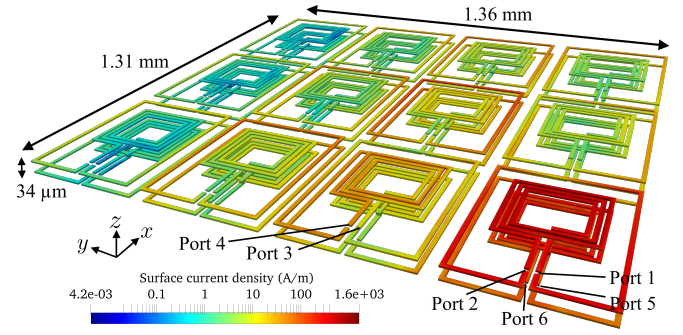


Fig. 16: Geometry and electric surface current density at 60 GHz for the inductor array in Section V-E.

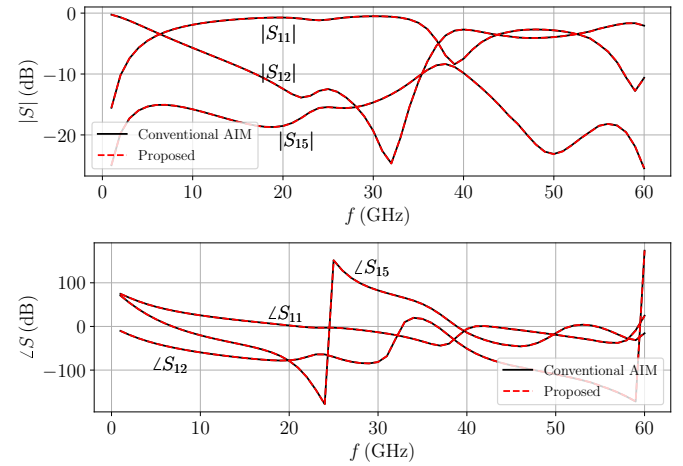


Fig. 17: Accuracy validation for the inductor array in Section V-E. Top panel: magnitude of S . Bottom panel: phase of S .

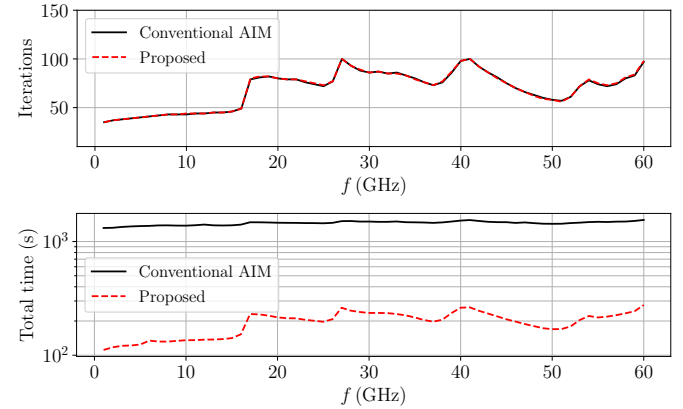


Fig. 18: Performance comparison for the inductor array in Section V-E. Top panel: iterations required for convergence. Bottom panel: CPU time per frequency.

lumped port excitation model was used [22], [60], with port definitions shown in Fig. 16, along with the computed electric surface current density at 60 GHz.

The top and bottom panels of Fig. 17 show, respectively, the magnitude and phase of S parameters corresponding to reflec-

tion, transmission, and coupling, for the proposed method and the conventional AIM. The proposed method is in excellent agreement in both magnitude and phase over the entire frequency range considered. Furthermore, the top panel of Fig. 18 confirms the effectiveness of the frequency-independent constraint preconditioner for all frequencies, while the bottom panel of Fig. 18 demonstrates the significant improvement in CPU time per frequency. The near-region direct integration times are shown in Table II, and the proposed method leads to a speed-up of $6.9\times$ in total, compared to the conventional AIM.

VI. DISCUSSION

Through various numerical examples, we demonstrated that the proposed method greatly speeds up frequency sweeps in SIE-based electromagnetic solvers without loss of accuracy. Specifically, we emphasize the following advantages arising from the use of the proposed technique:

- The cost-per-frequency of the matrix-fill and precorrection steps is eliminated. Instead, these steps need to be performed only once at the beginning of the frequency sweep.
- The computation of near-region interactions is greatly simplified, since they only involve static kernels. For layered media, the implication is that expensive Sommerfeld integration or approximation techniques such as the DCIM are avoided when computing near-region interactions.
- For complex geometries, there is usually a tradeoff between mesh quality and CPU time, since a high quality mesh may require more elements, which causes a significant increase in the CPU time associated with near-region interactions. The cost of using high-quality meshes is significantly alleviated with the proposed method, since near-region interactions are computed and precorrected only once.
- One may precompute and store to disk the static near-region matrix for a given structure. The matrix could be loaded and reused whenever needed, for example when further refinement is needed near a resonance, or when the frequency range must be extended.

VII. CONCLUSION

A novel technique is proposed for the accelerated electromagnetic modeling of large problems in homogeneous and layered media, based on an extended adaptive integral method (AIMx). The kernels of the SIE operators are decomposed into frequency-independent and frequency-dependent parts, such that the singularity of the kernel is contained entirely in the frequency-independent part. The frequency-dependent part is a smooth function which can be accurately interpolated, as shown with analytical and numerical error analyses. Therefore, matrix-vector products involving the frequency-dependent terms are fully accelerated with the AIM in both the near- and far-region. Only the near-region computations associated with the frequency-independent term need to be computed accurately with direct integration, which can be

performed in advance of a frequency sweep. This leads to significantly faster frequency sweeps. The efficiency of the proposed AIMx is demonstrated through diverse numerical examples, leading to total speed-ups ranging from $3\times$ to $16\times$.

REFERENCES

- [1] J.-M. Jin, *The Finite Element Method in Electromagnetics*, 3rd ed. Hoboken, NJ, USA: Wiley, 2014.
- [2] A. E. Ruehli, G. Antonini, and L. Jiang, *Circuit Oriented Electromagnetic Modeling Using the PEEC Techniques*. IEEE Press, 2017.
- [3] T. Moselhy, X. Hu, and L. Daniel, "pFFT in FastMaxwell: A fast impedance extraction solver for 3D conductor structures over substrate," in *Proc. Conf. Des., Automat. Test*, 2007.
- [4] S. Omar and D. Jiao, "A new volume integral formulation for broadband 3-D circuit extraction in inhomogeneous materials with and without external electromagnetic fields," *IEEE Trans. Microw. Theory Tech.*, vol. 61, no. 12, pp. 4302–4312, Dec. 2013.
- [5] A. Poggio and E. Miller, "Integral equation solutions of three-dimensional scattering problems," in *Computer Techniques for Electromagnetics*, ser. International Series of Monographs in Electrical Engineering. Pergamon, 1973, pp. 159 – 264.
- [6] W. Chai and D. Jiao, "Direct matrix solution of linear complexity for surface integral-equation-based impedance extraction of complicated 3-D structures," *Proc. IEEE*, vol. 101, no. 2, pp. 372–388, Jun. 2013.
- [7] Z.-G. Qian and W. C. Chew, "Fast full-wave surface integral equation solver for multiscale structure modeling," *IEEE Trans. Antennas Propag.*, vol. 57, no. 11, pp. 3594–3601, Nov. 2009.
- [8] T. Xia, H. Gan, M. Wei, W. C. Chew, H. Braunisch, Z. Qian, K. Aygün, and A. Aydiner, "An enhanced augmented electric-field integral equation formulation for dielectric objects," *IEEE Trans. Antennas Propag.*, vol. 64, no. 6, pp. 2339–2347, Jun. 2016.
- [9] M. Huynen, K. Y. Kapusuz, X. Sun, G. Van der Plas, E. Beyne, D. De Zutter, and D. Vande Ginste, "Entire domain basis function expansion of the differential surface admittance for efficient broadband characterization of lossy interconnects," *IEEE Trans. Microw. Theory Tech.*, vol. 68, no. 4, pp. 1217–1233, Jan. 2020.
- [10] S. Sharma and P. Triverio, "SLIM: A well-conditioned single-source boundary element method for modeling lossy conductors in layered media," *IEEE Antennas Wireless Propag. Lett.*, 2020 (submitted, arXiv: 2007.07378).
- [11] L. Greengard and V. Rokhlin, "A fast algorithm for particle simulations," *Journal of Computational Physics*, vol. 73, no. 2, pp. 325 – 348, 1987.
- [12] N. Engheta, W. D. Murphy, V. Rokhlin, and M. S. Vassiliou, "The fast multipole method (FMM) for electromagnetic scattering problems," *IEEE Trans. Antennas Propag.*, vol. 40, no. 6, pp. 634–641, Jun. 1992.
- [13] J. Song, C.-C. Lu, and W. C. Chew, "Multilevel fast multipole algorithm for electromagnetic scattering by large complex objects," *IEEE Trans. Antennas Propag.*, vol. 45, no. 10, pp. 1488–1493, Oct. 1997.
- [14] L. J. Jiang and W. C. Chew, "A mixed-form fast multipole algorithm," *IEEE Trans. Antennas Propag.*, vol. 53, no. 12, pp. 4145–4156, Dec. 2005.
- [15] E. Bleszynski, M. Bleszynski, and T. Jaroszewicz, "AIM: Adaptive integral method for solving large-scale electromagnetic scattering and radiation problems," *Radio Sci.*, vol. 31, no. 5, pp. 1225–1251, Sep. 1996.
- [16] K. A. Michalski and J. R. Mosig, "Multilayered media Green's functions in integral equation formulations," *IEEE Trans. Antennas Propag.*, vol. 45, no. 3, pp. 508–519, Mar. 1997.
- [17] F. Ling, J. Song, and J.-M. Jin, "Multilevel fast multipole algorithm for analysis of large-scale microstrip structures," *IEEE Microw. Guided Wave Lett.*, vol. 9, no. 12, pp. 508–510, Dec. 1999.
- [18] B. Hu and W. C. Chew, "Fast inhomogeneous plane wave algorithm for scattering from objects above the multilayered medium," *IEEE Trans. Geosci. Remote Sens.*, vol. 39, no. 5, pp. 1028–1038, May 2001.
- [19] V. Okhmatovski, M. Yuan, I. Jeffrey, and R. Phelps, "A three-dimensional precorrected FFT algorithm for fast method of moments solutions of the mixed-potential integral equation in layered media," *IEEE Trans. Microw. Theory Tech.*, vol. 57, no. 12, pp. 3505–3517, Dec. 2009.
- [20] F. Ling, C.-F. Wang, and J.-M. Jin, "An efficient algorithm for analyzing large-scale microstrip structures using adaptive integral method combined with discrete complex-image method," *IEEE Trans. Microw. Theory Tech.*, vol. 48, no. 5, pp. 832–839, May 2000.

- [21] K. Yang and A. E. Yilmaz, "A three-dimensional adaptive integral method for scattering from structures embedded in layered media," *IEEE Trans. Geosci. Remote Sens.*, vol. 50, no. 4, pp. 1130–1139, Apr. 2012.
- [22] S. Sharma, U. R. Patel, S. V. Hum, and P. Triverio, "A complete surface integral method for broadband modeling of 3D interconnects in stratified media," *arXiv e-prints*, p. arXiv: 1810.04030, Oct. 2018.
- [23] Z. Zhu, B. Song, and J. K. White, "Algorithms in FastImp: a fast and wide-band impedance extraction program for complicated 3-D geometries," *IEEE Trans. Comput.-Aided Design Integr. Circuits Syst.*, vol. 24, no. 7, pp. 981–998, Jul. 2005.
- [24] S. Q. Li, Y. Yu, C. H. Chan, K. F. Chan, and L. Tsang, "A sparse-matrix/canonical grid method for analyzing densely packed interconnects," *IEEE Trans. Microw. Theory Tech.*, vol. 49, no. 7, pp. 1221–1228, Jul. 2001.
- [25] B. J. Fassenfest, F. Capolino, D. R. Wilton, D. R. Jackson, and N. J. Champagne, "A fast MoM solution for large arrays: Green's function interpolation with FFT," *IEEE Antennas Wireless Propag. Lett.*, vol. 3, pp. 161–164, 2004.
- [26] S. M. Seo and J.-F. Lee, "A fast IE-FFT algorithm for solving PEC scattering problems," *IEEE Trans. Magn.*, vol. 41, no. 5, pp. 1476–1479, May 2005.
- [27] H. G. Wang and C. H. Chan, "The implementation of multilevel Green's function interpolation method for full-wave electromagnetic problems," *IEEE Trans. Antennas Propag.*, vol. 55, no. 5, pp. 1348–1358, May 2007.
- [28] D. Schobert and T. Eibert, "Direct field and mixed potential integral equation solutions by fast Fourier transform accelerated multilevel Green's function interpolation for conducting and impedance boundary objects," *Applied Computational Electromagnetics Society Journal*, vol. 26, pp. 1016–1023, Jan. 2011.
- [29] W. C. Gibson, *The Method of Moments in Electromagnetics*. Boca Raton, FL, USA: CRC press, 2014.
- [30] B. Fassenfest, J. D. Rockway, N. J. Champagne, and R. M. Sharpe, "A generalized fast frequency sweep algorithm for coupled circuit-EM simulations," in *IEEE Int. Symp. Antennas Propag.*, vol. 4, Sep. 2004, pp. 3944–3947.
- [31] T. Dhaene, J. Ureel, N. Fache, and D. De Zutter, "Adaptive frequency sampling algorithm for fast and accurate S-parameter modeling of general planar structures," in *Proc. of 1995 IEEE MTT-S Int. Microw. Symp.*, 1995, pp. 1427–1430 vol.3.
- [32] R. Lehmensiek and P. Meyer, "Creating accurate multivariate rational interpolation models of microwave circuits by using efficient adaptive sampling to minimize the number of computational electromagnetic analyses," *IEEE Trans. Microw. Theory Tech.*, vol. 49, no. 8, pp. 1419–1430, Aug. 2001.
- [33] G. Antonini, D. Deschrijver, and T. Dhaene, "Broadband rational macromodeling based on the adaptive frequency sampling algorithm and the partial element equivalent circuit method," *IEEE Trans. Electromagn. Compat.*, vol. 50, no. 1, pp. 128–137, Feb. 2008.
- [34] G. Antonini and D. Romano, "An accurate interpolation strategy for fast frequency sweep of partial element equivalent circuit models," *IEEE Trans. Electromagn. Compat.*, vol. 56, no. 3, pp. 653–658, Nov. 2014.
- [35] D. Colton and R. Kress, *Integral Equation Methods in Scattering Theory*. Hoboken, NJ, USA: Wiley, 1983.
- [36] S. Rao, D. Wilton, and A. Glisson, "Electromagnetic scattering by surfaces of arbitrary shape," *IEEE Trans. Antennas Propag.*, vol. 30, no. 3, pp. 409–418, May 1982.
- [37] M. M. Jia, S. Sun, Y. Li, Z. Qian, and W. C. Chew, "Acceleration of perturbation-based electric field integral equations using fast Fourier transform," *IEEE Trans. Antennas Propag.*, vol. 64, no. 10, pp. 4559–4564, Oct. 2016.
- [38] L. Lombardi, G. Antonini, and A. E. Ruehli, "Analytical evaluation of partial elements using a retarded Taylor series expansion of the Green's function," *IEEE Trans. Microw. Theory Tech.*, vol. 66, no. 5, pp. 2116–2127, May 2018.
- [39] K. Konno, Q. Chen, and R. J. Burkholder, "Fast computation of layered media Green's function via recursive Taylor expansion," *IEEE Antennas Wireless Propag. Lett.*, vol. 16, pp. 1048–1051, Oct. 2017.
- [40] S. Sharma, U. R. Patel, P. Triverio, "Accelerated electromagnetic analysis of interconnects in layered media using a near-field series expansion of the Greens function," in *IEEE Conf. Electr. Perform. Electron. Packag. and Syst.*, San Jose, CA, Oct. 2018.
- [41] W.-B. Ewe, L.-W. Li, Q. Wu, and M.-S. Leong, "Preconditioners for adaptive integral method implementation," *IEEE Trans. Antennas Propag.*, vol. 53, no. 7, pp. 2346–2350, Jul. 2005.
- [42] O. Wiedenmann and T. F. Eibert, "The effect of near-zone preconditioning on electromagnetic integral equations of first and second kind," *Advances in Radio Science*, vol. 11, pp. 61–65, 2013.
- [43] W. C. Chew, *Waves and Fields in Inhomogeneous Media*. Hoboken, NJ, USA: Wiley, 1999.
- [44] K. A. Michalski and D. Zheng, "Electromagnetic scattering and radiation by surfaces of arbitrary shape in layered media. i. theory," *IEEE Trans. Antennas Propag.*, vol. 38, no. 3, pp. 335–344, Mar. 1990.
- [45] K. A. Michalski and J. R. Mosig, "Efficient computation of Sommerfeld integral tails - methods and algorithms," *Journal of Electromagnetic Waves and Applications*, vol. 30, no. 3, pp. 281–317, 2016.
- [46] M. I. Aksun, "A robust approach for the derivation of closed-form green's functions," *IEEE Trans. Microw. Theory Tech.*, vol. 44, no. 5, pp. 651–658, May 1996.
- [47] E. Simsek, Q. H. Liu, and B. Wei, "Singularity subtraction for evaluation of green's functions for multilayer media," *IEEE Trans. Microw. Theory Tech.*, vol. 54, no. 1, pp. 216–225, Jan. 2006.
- [48] K. Yang and A. E. Yilmaz, "Comparison of precorrected FFT/adaptive integral method matching schemes," *Microwave and Optical Technology Letters*, vol. 53, no. 6, pp. 1368–1372, Jun. 2011.
- [49] M. Abramowitz and I. A. Stegun, *Handbook of Mathematical Functions with Formulas, Graphs, and Mathematical Tables*, 10th ed. New York: Dover, 1964.
- [50] S. Sharma and P. Triverio, "A fully-accelerated surface integral equation method for the electromagnetic modeling of arbitrary objects," *IEEE Trans. Antennas Propag.*, 2020 (submitted, arXiv: 2003.11679).
- [51] The Sage Developers, *SageMath, the Sage Mathematics Software System (Version 9.1)*, 2020, <https://www.sagemath.org>.
- [52] S. Balay, S. Abhyankar, M. F. Adams, J. Brown, P. Brune, K. Buschelman, L. Dalcin, V. Eijkhout, W. D. Gropp, D. Kaushik, M. G. Knepley, D. A. May, L. C. McInnes, R. T. Mills, T. Munson, K. Rupp, P. Sanan, B. F. Smith, S. Zampini, H. Zhang, *PETSc Web Page*. (2019). Accessed: Nov. 01, 2019. Available: <http://www.mcs.anl.gov/petsc>.
- [53] Y. Saad and M. Schultz, "GMRES: A generalized minimal residual algorithm for solving nonsymmetric linear systems," *SIAM J. Scientific Statistical Comput.*, vol. 7, no. 3, pp. 856–869, 1986.
- [54] A. C. Woo, H. T. G. Wang, M. J. Schuh, and M. L. Sanders, "EM programmer's notebook-benchmark radar targets for the validation of computational electromagnetics programs," *IEEE Antennas Propag. Mag.*, vol. 35, no. 1, pp. 84–89, Feb. 1993.
- [55] U. R. Patel, P. Triverio, and S. V. Hum, "A macromodeling approach to efficiently compute scattering from large arrays of complex scatterers," *IEEE Trans. Antennas Propag.*, vol. 66, no. 11, pp. 6158–6169, Nov. 2018.
- [56] C. Geaney, M. Hosseini, and S. Hum, "A cascaded polarizer/reflectarray for independent dual circular polarization control," *ESA Antenna Workshop on Antennas and RF Systems for Space Science, Noordwijk, Netherlands, Oct. 2017*, Oct. 2017.
- [57] B. G. Duffley, G. A. Morin, M. Mikavica, and Y. M. M. Antar, "A wide-band printed double-sided dipole array," *IEEE Trans. Antennas Propag.*, vol. 52, no. 2, pp. 628–631, Feb. 2004.
- [58] U. R. Patel, S. Sharma, S. Yang, S. V. Hum, and P. Triverio, "Full-wave electromagnetic characterization of 3D interconnects using a surface integral formulation," in *IEEE Conf. Electr. Perform. Electron. Packag. and Syst.*, San Jose, CA, Oct. 2017.
- [59] S. V. Yuferev and N. Ida, *Surface Impedance Boundary Conditions: A Comprehensive Approach*. Boca Raton, FL, USA: CRC Press, 2009.
- [60] Y. Wang, D. Gope, V. Jandhyala, and C.-J. R. Shi, "Generalized Kirchoff's current and voltage law formulation for coupled circuit-electromagnetic simulation with surface integral equations," *IEEE Trans. Microw. Theory Tech.*, vol. 52, no. 7, pp. 1673–1682, Jul. 2004.